Chemical Science

ROYAL SOCIETY OF CHEMISTRY

EDGE ARTICLE

View Article Online
View Journal | View Issue

Cite this: *Chem. Sci.*, 2025, **16**, 22160

All publication charges for this article have been paid for by the Royal Society of Chemistry

Single atom-bridged Au nanozymes boost glucose oxidase-like activity in acidic media

Xin Luo,†[a] Feilong Tan,†[a] Zhenglong Mao,[a] Yan Zhang,[a] Yinjun Tang,[b] Canglong Wang,[e] Wenling Gu,[b] Cao Li,[a] Juewen Liu *[c] and Chengzhou Zhu *[bd]

Although Au nanozymes hold great promise as glucose oxidase (GOx) mimics, their catalytic activity and pH dependence remain significant challenges. Herein, we synthesize Fe single atom bridged Au nanozymes (Au_{NPs}/FeNC) with dual catalytic sites, achieving a 3.7-fold enhancement in GOx-like activity under acidic media compared to Au_{NPs}/NC. Experimental and theoretical analyses reveal that charge transfer from Au to Fe single atom facilitates O_2 adsorption at Fe sites, synergistically boosting glucose oxidation. Unlike previously reported Au–H intermediates formed under alkaline conditions, *in situ* monitoring identifies the formation of Au–Fe–OO intermediates in Au_{NPs}/FeNC, which facilitate the dehydrogenation of glucose and enhance the catalytic efficiency in acidic environments. Benefiting from optimal GOx- and peroxidase-like activities at pH 4.0, an Au_{NPs}/FeNC-based glucose cascade system is constructed with exceptional properties. As a proof of concept, this system is integrated into a portable, gel-based sensor for real-time and visual determination of organophosphorus pesticides. This study provides valuable insights into the rational design of high-performance nanozymes featuring dual catalytic sites for advanced sensing applications.

Received 21st July 2025
Accepted 12th October 2025

DOI: 10.1039/d5sc05430c

rsc.li/chemical-science

Introduction

Glucose oxidase (GOx), with its exceptional catalytic efficiency and substrate specificity, plays a pivotal role in bioassays and biomedicine.[1–3] However, its practical applications are hindered by intrinsic drawbacks such as poor stability, high production costs, and short shelf life.[4–6] Nanozymes, artificial enzymes with intrinsic enzyme-catalytic activities, have emerged as promising alternatives owing to their structural stability, cost-effectiveness, and adjustable activity.[7–11] Among them, Au nanoparticles (NPs) have emerged as particularly promising GOx mimics, catalyzing glucose oxidation to generate H_2O_2, a critical molecule in biosensing and disease diagnosis.[12–15] However, the GOx-like activity of currently reported Au nanozymes remains unsatisfactory owing to their insufficient intrinsic activity.[16,17] Moreover, their underlying mechanisms are not yet fully elucidated.[18,19] Therefore, the development of novel Au nanozymes with enhanced catalytic performance is highly desirable and remains a priority for advancing practical applications.

Recently, extensive efforts have been devoted to optimizing the catalytic performance of Au nanozymes.[20,21] Carbon-based materials, for instance, have been widely explored as catalyst supports for Au NPs due to their ability to establish strong metal–support interactions, facilitate mass/charge transfer, and improve catalytic efficiency.[22–24] Additionally, doping Au with other metals has emerged as an effective strategy to tune its electronic configuration and enhance GOx-like activity.[25,26] Despite these advances, the GOx-like activity of Au nanozymes remains predominantly restricted to alkaline media, with limited catalytic efficiency and mechanistic understanding in acidic or neutral conditions.[27–29] In natural GOx, a histidine (His) residue serves as a Brønsted base, initially abstracting the C1 hydroxyl proton from glucose, thereby facilitating glucose oxidation (Fig. 1a).[30,31] Similarly, mechanistic investigations suggest that traditional Au nanozymes follow a comparable reaction pathway, with OH^- ions acting as the Brønsted base and O_2 serving as the terminal electron acceptor (Fig. 1b).[32–34]

[a]*National "111" Center for Cellular Regulation and Molecular Pharmaceutics, Key Laboratory of Fermentation Engineering (Ministry of Education), Cooperative Innovation Center of Industrial Fermentation (Ministry of Education & Hubei Province), School of Life and Health Sciences, Hubei University of Technology, Wuhan 430068, P. R. China*

[b]*State Key Laboratory of Green Pesticide, International Joint Research Center for Intelligent Biosensing Technology and Health, College of Chemistry, Central China Normal University, Wuhan 430079, P. R. China. E-mail: czzhu@ccnu.edu.cn*

[c]*Department of Chemistry, Waterloo Institute for Nanotechnology, University of Waterloo, 200 University Avenue West, Waterloo, Ontario, N2L 3G1, Canada. E-mail: liujw@uwaterloo.ca*

[d]*College of Material Chemistry and Chemical Engineering, Key Laboratory of Organosilicon Chemistry and Material Technology, Ministry of Education, Hangzhou Normal University, Hangzhou 311121, P. R. China*

[e]*Institute of Modern Physics, Chinese Academy of Science, Lanzhou 730000, P. R. China*

† These authors contributed equally to this work.

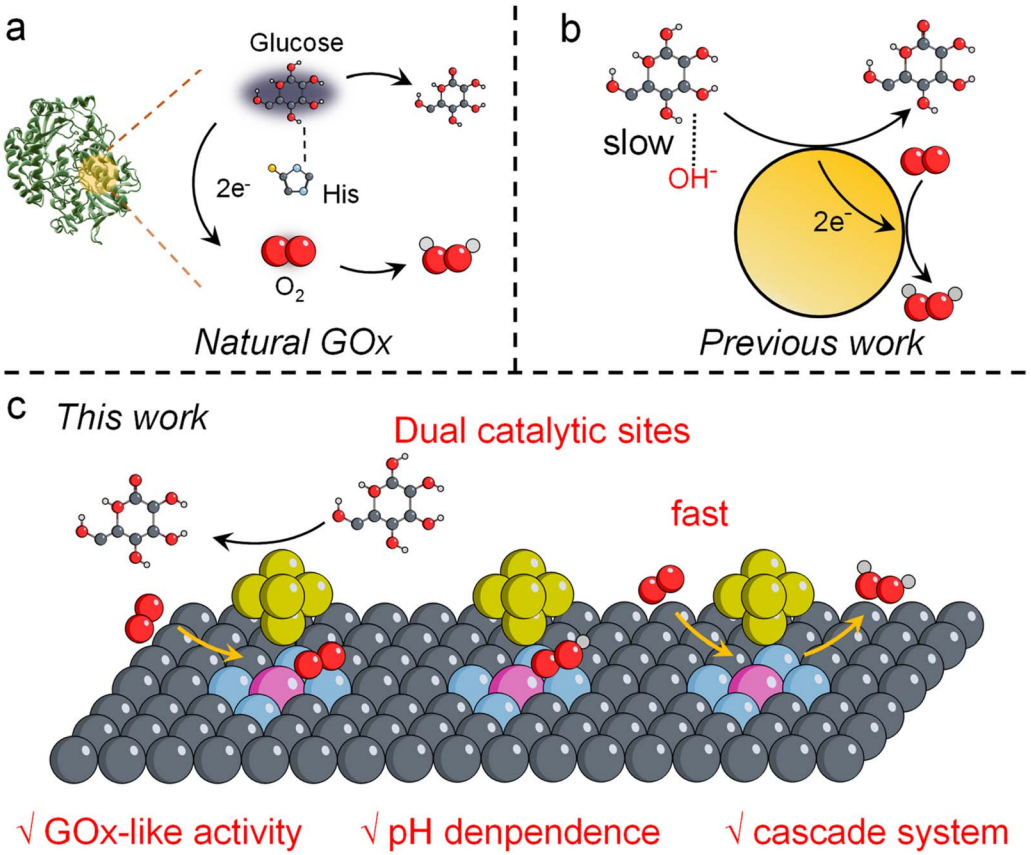

Fig. 1 Design principles of this work. (a) Schematic diagrams of the catalysis model of natural GOx. (b) Scheme of GOx-mimicking nanozymes with single catalytic sites. (c) Scheme of GOx-mimicking nanozymes with dual catalytic sites.

Consequently, the overall reaction rate is governed by the dehydrogenation of glucose. However, the continuous generation of gluconic acid progressively depletes OH^- ions, leading to catalytic slowdown. To this end, the rational design of catalytic centers to boost glucose oxidation while overcoming pH constraints is of paramount importance.

In this work, we design Fe single atom (SA)-bridged Au nanozymes (Au_{NPs}/FeNC) with dual catalytic sites to overcome the pH-dependence limitations of GOx-like activity (Fig. 1c), which exhibit a 3.7-fold enhancement in acidic media in comparison to Au_{NPs}/NC. Fe SAs on the N-doped carbon serve as anchoring sites for Au NPs, establishing strong interactions that provide an Au–Fe charge transfer pathway and facilitate O_2 adsorption. Notably, *in situ* experiments provide the first direct visualization of Au–Fe–OO intermediates, rather than conventional Au–H intermediates, during glucose oxidation. Based on these insights, a plausible mechanism for glucose oxidation is proposed in which the reaction bypasses OH^--dependence pathways, allowing for efficient catalysis in acidic media. Leveraging the aligned optimal conditions at pH 4.0 for both GOx- and peroxidase (POD)-like activity, Au_{NPs}/FeNC enable an efficient glucose cascade catalysis system, further applied in a portable, gel-based biosensor for real-time, visual determination of organophosphorus pesticides (OPs) in the range of 10–1000 ng mL^{-1}, with a low limit of detection (LOD) of 1.9 ng mL^{-1}.

Results and discussion

FeNC was synthesized *via* pyrolysis of a mixture of glucosamine and $FeCl_3$ in the presence of dual templates of SiO_2 and $ZnCl_2$. Subsequently, $HAuCl_4$ served as the Au source for the *in situ* growth of Au to obtain Au_{NPs}/FeNC. For comparison, Au_{NPs} & FeNC were obtained by physically mixing FeNC with Au_{NPs}. Fig. 2a reveals that distinct black particles are uniformly distributed on the carbon support. Energy-dispersive spectroscopy (EDS) mapping images further demonstrate that Au is primarily localized within the particles, whereas Fe is randomly dispersed across the carbon support (Fig. S1). High-resolution TEM (HRTEM) image (Fig. 2b) shows a lattice spacing of 0.208 nm, corresponding to the (111) plane of Au. Furthermore, the aberration-corrected high-angle annular dark-field scanning transmission electron microscopy (AC-HADDF-STEM) image (Fig. 2c) reveals the abundant Fe SAs on the support of Au_{NPs}/FeNC. The crystalline phases of the samples analyzed through X-ray diffraction (XRD) patterns reveal no characteristic metal peaks for FeNC (Fig. S2), while Au_{NPs}/FeNC displays distinct peaks matching the standard peaks of Au (JCPDS-04-0784). N_2 adsorption–desorption isotherm analysis indicates a surface area of 199 $m^2\ g^{-1}$ and abundant mesopores in Au_{NPs}/FeNC (Fig. S3), which facilitate substrate and product diffusion as well as efficient electron transport during catalytic reactions. X-ray photoelectron spectroscopy (XPS) was utilized to

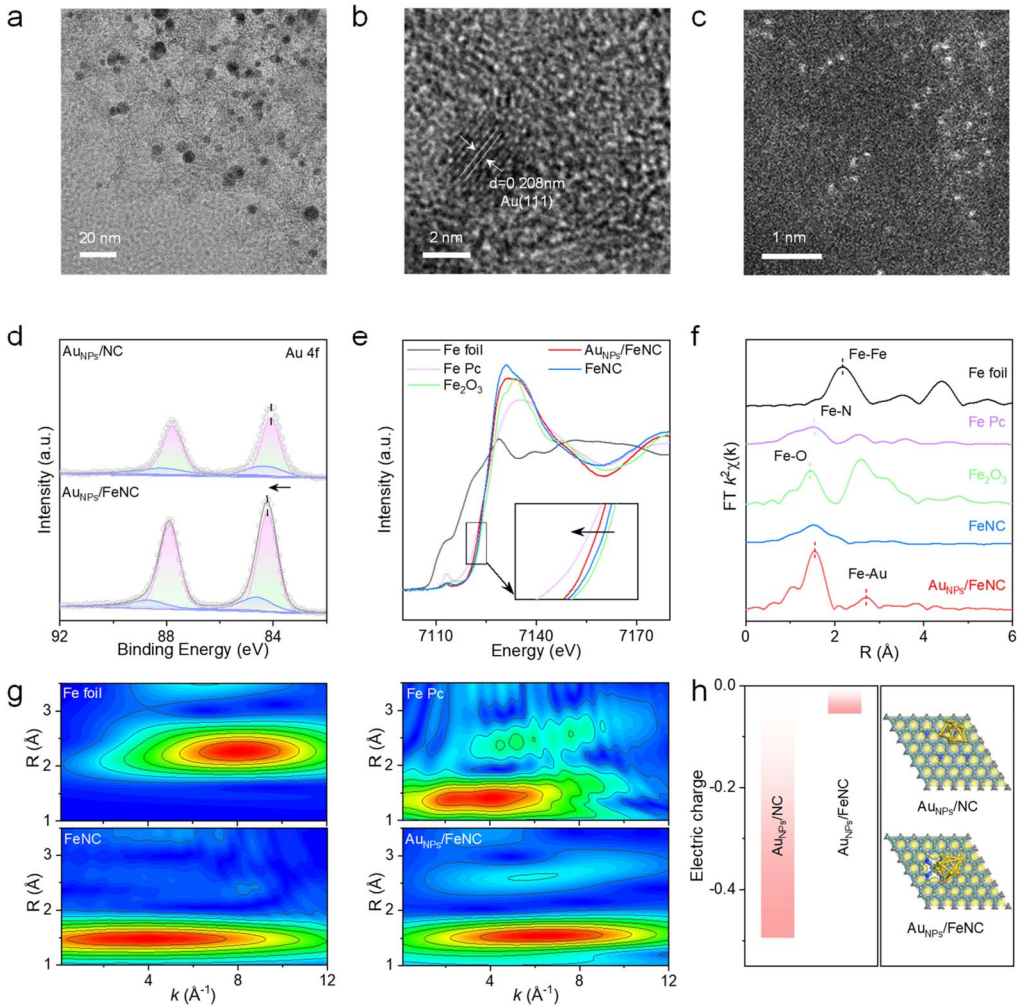

Fig. 2 (a) TEM, and (b) HRTEM images of Au_{NPs}/FeNC. (c) AC-HAADF-STEM image in the region of the carbon substrate of Au_{NPs}/FeNC. (d) XPS spectra of Au 4f for Au_{NPs}/NC and Au_{NPs}/FeNC. (e) XANES spectra of Au_{NPs}/FeNC, FeNC, Fe foil, Fe Pc, and Fe_2O_3. (f) The corresponding Fourier-transformed Fe K-edge EXAFS spectra. (g) Wavelet transforms for the k^3-weighted Fe K-edge EXAFS signals of Fe foil, Fe Pc, FeNC, and Au_{NPs}/FeNC. (h) The electric charge of Au sites in Au_{NPs}/NC and Au_{NPs}/FeNC.

investigate chemical composition. The N 1s spectrum of Au_{NPs}/FeNC is deconvoluted into pyridinic N, Fe–N, pyrrolic N, and graphite N components (Fig. S4).[35] Notably, the Au 4f peak in Au_{NPs}/FeNC shifts slightly toward higher binding energy compared to Au_{NPs}/NC (Fig. 2d), suggesting that the introduction of Fe SAs enables electron transfer from Au_{NPs} to the support. To further elucidate the electronic structure of Au_{NPs}/FeNC, X-ray absorption near-edge structure (XANES) and X-ray absorption fine structure (EXAFS) analyses were employed. In the Fe K-edge spectra, the absorption edges of Fe K-edge XANES curves in Au_{NPs}/FeNC and FeNC fall between those of iron phthalocyanine (Fe Pc) and Fe_2O_3. Additionally, the absorption edge of Au_{NPs}/FeNC exhibits a negative shift relative to FeNC, suggesting electron transfer from Au_{NPs} to Fe sites (Fig. 2e). Fourier transformed (FT) k^3-weighted EXAFS spectra of Au_{NPs}/FeNC display a primary peak at 1.63 Å, attributed to the Fe–N bond, without evidence of Fe–Fe bond at 2.18 Å (Fig. 2f). Additionally, a peak at around 2.7 Å is observed in Au_{NPs}/FeNC but not in FeNC, illustrating the formation of the Fe–Au bond in Au_{NPs}/FeNC. EXAFS fitting results (Fig. S5 and Table S1) indicate a Fe–N coordination number of 3.95 with a bond length of 2.01 Å, suggesting a Fe–N_4 configuration in Au_{NPs}/FeNC. In addition, wavelet transform (WT) analysis further confirms the coordination of the Fe–N coordination structure of Au_{NPs}/FeNC (Fig. 2g). Additionally, the Au EXAFS curve of AuNPs/FeNC in Fig. S6 exhibits the main peak at around 1.95 and 2.42 Å, associated with the Au–Fe and Au–Au interactions, respectively.[36] To explore the electronic properties, density functional theory (DFT) calculations were conducted. As shown in Fig. 2h, the electric charge at Au sites in Au_{NPs}/FeNC ($-0.055e$) is higher than that in Au_{NPs}/NC ($-0.494e$), indicating that the introduction of Fe SAs facilitates electron transfer from Au_{NPs} to the substrate, leading to a redistribution of electrons at the catalytic centers, consistent with the experimental results. Ultraviolet photoelectron spectroscopy (UPS) was employed to better understand the band structure information of nanozymes (Fig. S7). Notably, the cutoff energy of Au_{NPs}/FeNC and Au_{NPs}/NC is 16.76 and 16.62 eV, respectively. The calculated work

functions are 4.46 eV for Au_{NPs}/FeNC and 4.60 eV for Au_{NPs}/NC, indicating that Au_{NPs}/FeNC more readily donate electrons to reaction intermediates.[37]

Fig. 3a presents a schematic illustration of the reaction catalyzed by Au_{NPs}/FeNC, where O_2 adsorption and activation realize the glucose cascade reaction. To explore the ability to mimic GOx, the glucose-nanozyme supernatant was assessed using a horseradish peroxidase (HRP)-based colorimetric system with 3,3,5,5-tetramethyl-benzidine (TMB) as the chromogenic substrate.[38] As shown in Fig. 3b, the glucose-like activity of Au_{NPs}/FeNC is 3.7- and 2.9-fold higher than that of Au_{NPs}/NC and Au_{NPs} & FeNC. To further explore the GOx-like property, the production of glucose acid was evaluated by adding hydroxylamine and Fe^{3+} to the reaction supernatant.[39] As displayed in Fig. 3c, the absorbance band in both Au_{NPs}/FeNC and GOx confirms the presence of gluconic acid, demonstrating the GOx-like behavior of Au_{NPs}/FeNC. Additionally, Au_{NPs}/FeNC exhibit 2.2-fold higher intensity than Au_{NPs}/NC, suggesting that the introduction of Fe SAs facilitates the generation of gluconic acid. To further investigate the specificity mechanism, the activation energy (E_a) of glucose catalysis was calculated according to the Arrhenius equation. In a chemical reaction, E_a represents the minimum energy required for reactants to reach the activated state and is closely related to the reaction rate.[40] The E_a value for Au_{NPs}/FeNC is 1.15 kJ mol^{-1}, lower than that of Au_{NPs}/NC (6.46 kJ mol^{-1}) and Au_{NPs} & FeNC (8.33 kJ mol^{-1}), indicating its superior glucose catalytic efficiency (Fig. 3d). Similar to natural GOx, the GOx-like activity of Au_{NPs}/FeNC is pH-dependent. As revealed in Fig. 3e, its optimal GOx-like activity is observed at pH 4.0, aligning with its optimal POD-

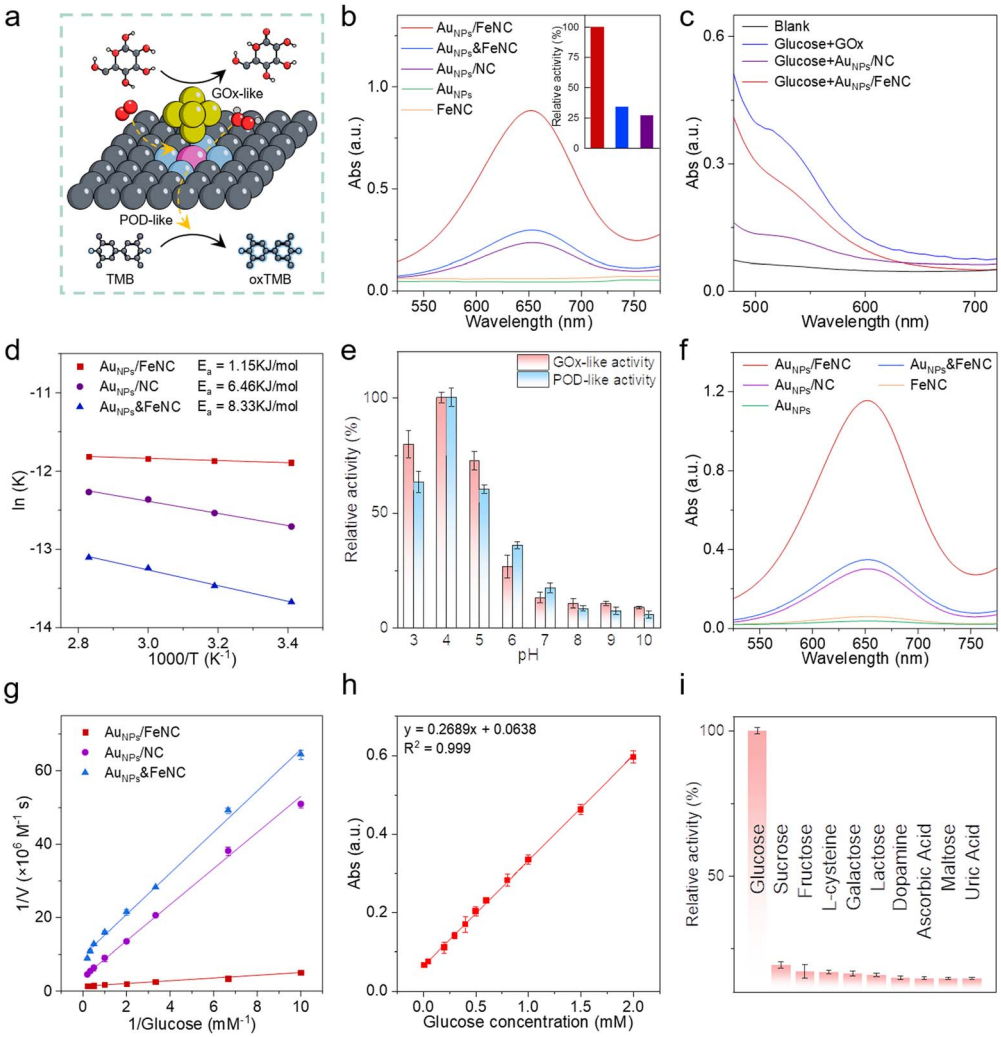

Fig. 3 (a) Schematic illustration of glucose cascade reaction on Au_{NPs}/FeNC. (b) Absorbance spectra of the glucose-nanozyme supernatant catalyzed by the HRP-TMB system. (c) Absorbance spectra of gluconic acid-specific colorimetric assay catalyzed by Au_{NPs}/FeNC and GOx. (d) Arrhenius plots of ln(*k*) *versus* 1000/*T* for Au_{NPs}/FeNC, Au_{NPs}/NC, and Au_{NPs} & FeNC. (e) The GOx- and POD-like activity of Au_{NPs}/FeNC at different pH levels. (f) Absorbance spectra of glucose-TMB catalyzed by Au_{NPs}/FeNC, Au_{NPs} & FeNC, Au_{NPs}/NC, FeNC, and Au_{NPs}. (g) The corresponding Lineweaver–Burk plots with glucose as a substrate. (h) The linear calibration plots of Au_{NPs}/FeNC cascade system for glucose detection (0.01, 0.05, 0.2, 0.3, 0.4, 0.5, 0.6, 0.8, 1, 1.5, 2 mM). (i) Selectivity evaluation for Au_{NPs}/FeNC cascade system. Error bars represent mean ± SD ($n = 3$).

like activity. Consequently, the Au_{NPs}/FeNC cascade system shows superior catalytic activity under the same acidic conditions (Fig. S8a). Additionally, the GOx-like activity of Au_{NPs} increased with increasing pH, implying that the introduction of Fe SAs regulates the catalytic centers (Fig. S8b). Regarding POD-like activity, Au_{NPs}/FeNC, Au_{NPs} & FeNC, and FeNC display significantly higher POD-like activity than Au_{NPs}/NC (Fig. S9a), highlighting Fe SAs as the primary active sites for H_2O_2 activation. Notably, the introduction of Au_{NPs} slightly enhances the POD-like activity of Au_{NPs}/FeNC, which is 8.7 times greater than its oxidase-like activity (Fig. S9b), indicating a remarkable preference for POD-like activity. To validate the cascade catalytic activity, a colorimetric assay was conducted (Fig. 3f). The absorbance at 652 nm for the Au_{NPs}/FeNC cascade system is 3.8-fold higher than that of Au_{NPs}/NC, indicating that the introduction of Fe SAs significantly enhances the catalytic efficiency. Interestingly, the cascade catalytic activity of Au_{NPs}/FeNC is 3.3-fold higher than that of Au_{NPs} & FeNC, whereas its POD-like activity is slightly higher than that of Au_{NPs} & FeNC. This result suggests that Fe SA-bridged Au NPs significantly optimize the activation efficiency of the glucose cascade system. When glucose is the only substrate, the GOx–HRP system produces oxTMB (Fig. S10), whereas neither the GOx nor HRP system alone does, suggesting that Au_{NPs}/FeNC possess both GOx- and HRP-like catalytic activities. To quantitatively evaluate the catalytic performance of the biomimetic cascade system, a typical Michaelis–Menten kinetic analysis was conducted. As shown in Fig. 3g and Table S2, the maximum reaction velocity (V_{max}) of Au_{NPs}/FeNC for the glucose cascade system is calculated to be 75.6×10^{-8} M s^{-1}, which is 2.9-fold and 6.9-fold higher than that of Au_{NPs}/NC and Au_{NPs} & FeNC. Moreover, Au_{NPs}/FeNC possess the smallest Michaelis–Menten constants (K_m) of 0.28 mM, indicating their superior affinity for glucose. Benefiting from the highly compatible pH conditions of Au_{NPs}/FeNC with both GOx- and POD-like activities, the engineered Au_{NPs}/FeNC-based cascade catalysis system was applied for the sensitive and selective colorimetric detection of glucose. As shown in Fig. 3h, the absorbance of oxTMB at 652 nm increases progressively with glucose concentration, exhibiting a good linear correlation in the range of 0.01–2 mM with a LOD of 2.9 μM. Furthermore, Au_{NPs}/FeNC show outstanding recyclability (Fig. S11), maintaining nearly constant glucose oxidation activity after five catalytic cycles. In addition, the biomimetic Au_{NPs}/FeNC system displays satisfactory selectivity for glucose over common interfering substances, including sucrose, fructose, L-cysteine, galactose, lactose, dopamine, ascorbic acid, maltose, and uric acid (Fig. 3i).

To investigate the catalytic mechanism of glucose oxidation, DFT calculations were performed to study glucose adsorption on the nanozymes. Fig. S12a reveals that the adsorption energy of glucose on the Au_{NPs}/FeNC model (−2.06 eV) is lower than that on the Au_{NPs}/NC model (−1.90 eV), indicating that the introduction of Fe SAs is favorable for glucose adsorption. In the Au_{NPs}/FeNC model, the adsorption energy of O_2 at the Fe sites (−0.94 eV) is lower than that at the Au sites (−0.39 eV), suggesting that Fe sites are more favorable for O_2 adsorption (Fig. 4a). The projected state density (PDOS) analysis for Au_{NPs}/FeNC and Au_{NPs}/NC (Fig. 4b) reveals enhanced orbital hybridizations between Fe and C in Au_{NPs}/FeNC, consistent with its stronger glucose adsorption capacity. Mulliken charge analysis (Fig. S12b) indicates that the charge transfer from glucose to Au_{NPs}/FeNC is 0.123*e*, higher than that to Au_{NPs}/NC (0.104*e*), verifying that the introduction of Fe SAs optimizes the interfacial charge transfer process. To elucidate reaction pathways and identify intermediates, *in situ* attenuated total reflection-FTIR (ATR-FTIR) experiments were conducted for Au_{NPs}/NC and Au_{NPs}/FeNC under reaction conditions (Fig. 4c and d). Upon glucose introduction, a distinct signal peak at 1573 cm^{-1}, corresponding to O–C–O bending, confirms the formation of gluconate.[41] The intensity of this peak is significantly higher than for Au_{NPs}/NC, suggesting enhanced glucose oxidation. A peak at 1639 cm^{-1} corresponds to the H–O–H bending, while the peak at 1279 cm^{-1} is attributed to the O–O stretching mode of adsorbed OOH (*OOH).[42,43] In addition, the band at 1410 cm^{-1} is assigned to adsorbed O_2, observed exclusively in Au_{NPs}/FeNC, indicating that the introduction of Fe SAs facilitates O_2 absorption on the surface of Au_{NPs}/FeNC.[44] Notably, Fe–O and *OOH species, represented by peaks at 653 and 930 cm^{-1}, are unique to AuNPs/FeNC. Furthermore, the *OO species absorption band at 1018 cm^{-1} shifts to a lower frequency in Au_{NPs}/FeNC compared to Au_{NPs}/NC, indicating a stronger Fe–O interaction that enhances O–O bond polarization.[45] To monitor real-time catalytic processes, *in situ* electron paramagnetic resonance (EPR) measurement was conducted. As displayed in Fig. 4e, in Au_{NPs}, an initial $^{\cdot}H$ signal at 20 s transitions into a $^{\cdot}OOH$ signal at 100 s, with increasing intensity facilitating H_2O_2 formation. In contrast, Au_{NPs}/FeNC follow a distinct radical pathway, transitioning from $O_2^{\cdot-}$ to $^{\cdot}OOH$. To further verify these findings, 2,2,6,6-tetramethylpiperidinooxy (TEMPO) was employed as a hydrogen-extracting reagent.[46] The catalytic activity of Au_{NPs} decreases by 89% in the presence of TEMPO, whereas Au_{NPs}/FeNC exhibits no significant decrease (Fig. S13), demonstrating that the crucial role of surface Au–H species in glucose oxidation by Au_{NPs} and suggesting an alternative catalytic pathway in Au_{NPs}/FeNC. Based on these findings, a plausible reaction mechanism is proposed (Fig. 4f). In Au_{NPs}, OH^- acts as a Brønsted base, initially abstracting H^+ from the C1 hydroxyl group of glucose. Subsequently, certain Au atoms extract H from the glucose C–H bond, forming Au–H intermediates. Then, O_2 accepts electrons, becoming activated and integrating into Au–H to form Au–OOH species, which ultimately dissociate to generate H_2O_2. In contrast, under a proton-rich acidic environment, glucose first adsorbs onto the Au sites of Au_{NPs}/FeNC. Subsequently, the electron-rich Fe sites adsorb O_2 to form *OO intermediates. The Au–Fe–OO intermediates then combine with H^+ derived from glucose, forming Au–Fe–OOH species. The *OOH at the Fe sites further extracts H from the C–H bond of glucose to generate $*H_2O_2$, thereby completing the catalytic cycle and enabling efficient glucose oxidation in acidic conditions.

Leveraging the exceptional glucose cascade system of Au_{NPs}/FeNC, a colorimetric assay is developed as a proof-of-concept application for AChE and OP detection. AChE catalyzes the hydrolysis of acetylthiocholine (ATCh) into thiocholine (TCh),

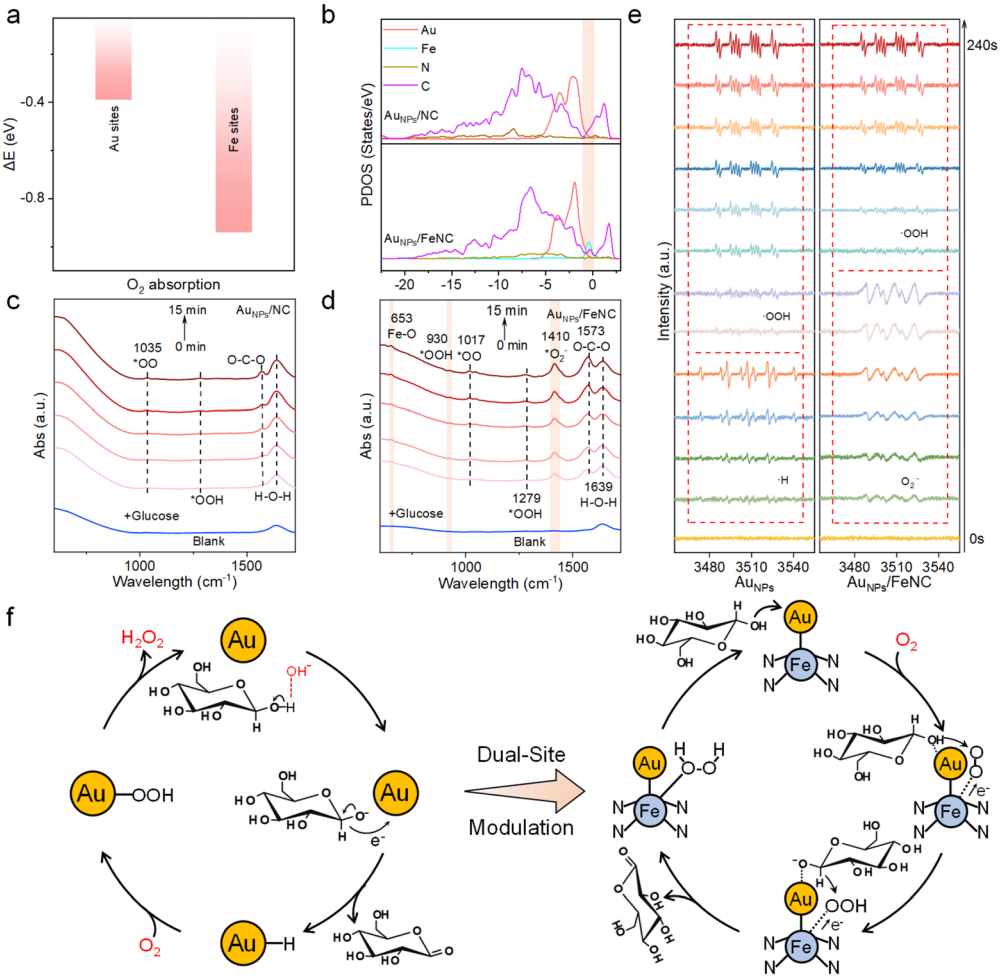

Fig. 4 (a) Adsorption energies of the O_2 molecule adsorption on Au and Fe sites in Au_{NPs}/FeNC model. (b) PDOS profiles of Au_{NPs}/FeNC and Au_{NPs}/NC structures. *In situ* ATR-FTIR spectra of the glucose oxidation reaction on (c) Au_{NPs}/NC and (d) Au_{NPs}/FeNC. (e) *In situ* EPR spectra of Au_{NPs} (under alkaline conditions) and Au_{NPs}/FeNC (under acid conditions) during catalytic glucose oxidation. (f) Mechanism of glucose catalyzed by Au_{NPs} (under alkaline conditions) and Au_{NPs}/FeNC (under acid conditions).

which is essential for regulating the neurotransmitter acetylcholine levels.[47] TCh, a sulfhydryl molecule, binds the active sites of Au_{NPs}/FeNC, thereby inhibiting the biomimetic cascade reaction. Au anchors mercapto molecules *via* the Au–S bond. To confirm this inhibitory effect, cysteine (Cys) and glutathione (GSH) were introduced into the FeNC–H_2O_2 system, resulting in a noticeable decrease in absorbance (Fig. S14), suggesting that the active sites of FeNC were effectively blocked by the mercapto molecules.[48] Leveraging the enzyme-like inhibitory mechanism of active sites, an Au_{NPs}/FeNC-based biosensor was constructed to further evaluate its sensitivity to AChE activity. As shown in Fig. S15a, the catalytic activity of Au_{NPs}/FeNC gradually decreases with increasing AChE concentrations in the presence of ATCh (5 mM). The Au_{NPs}/FeNC-based biosensor displays a good linear relationship between the absorbance of oxTMB and AChE concentrations in the range of 0.5 to 50 mU mL^{-1} with an LOD of 0.16 mU mL^{-1} (Fig. S15b). Notably, the Au_{NPs}/FeNC-based biosensor displays a broader detection range compared to the Au_{NPs}/NC-based biosensor, suggesting that the introduction of Fe SAs enhances the sensitivity and detection performance of biosensors.

OPs can rapidly inhibit the AChE activity, leading to nervous system dysfunction. In this study, fenthion was selected as a model OP due to its inhibition effect on AChE activity, consistent with observations of the Au_{NPs}/FeNC system (Fig. S16). Compared with Au_{NPs}/NC-based biosensor, Au_{NPs}/FeNC-based biosensor exhibits a wider detection range for OP detection (Fig. S17), indicating the main role of Fe single atoms. To realize visual, rapid, and real-time detection, a portable, smartphone-integrated gel biosensor was developed for the quantitative OP analysis. As illustrated in Fig. 5a, agarose hydrogels were formed on the snap caps of EP tubes by immersing them in a solution containing Au_{NPs}/FeNC and TMB. When OPs were introduced into the EP tube lumen along with AChE for 5 min, the tubes were inverted, causing a color shift from colorless to blue. The color intensity was captured using the smartphone app ColorDesk, which quantified the results obtained by converting images into RGB values. As shown in Fig. 5b, the biosensor exhibits a progressive blue shift with

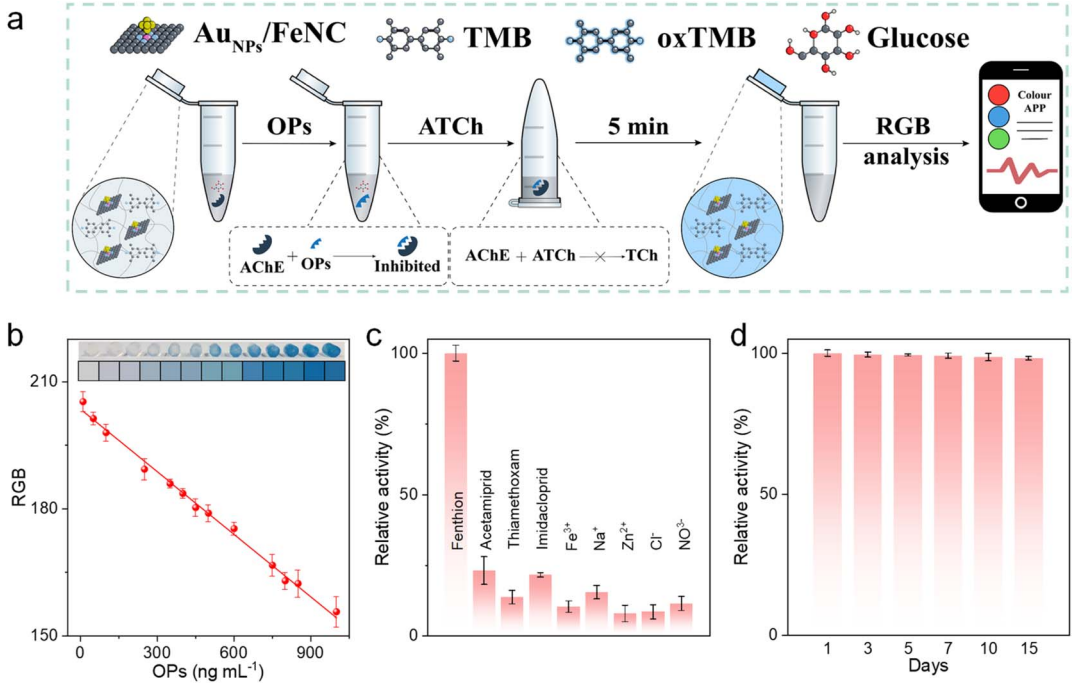

Fig. 5 (a) Schematic illustration of the smartphone-assisted sensing of OPs using a gel-based biosensor. (b) The calibration curves of the RGB value toward the different concentrations of OPs. (c) The selectivity test and (d) the long-term storage stability of gel-based biosensors. Error bars represent mean ± SD (n = 3).

increasing OP concentrations, detectable by the naked eye. Linear regression reveals a strong correlation between the RGB values and OP concentrations within the range of 10 to 1000 ng mL^{-1}, with a calculated LOD of 1.9 ng mL^{-1}. Compared to other OP sensing platforms, the Au$_{NPs}$/FeNC-based gel biosensor kit exhibits competitive sensitivity (Table S3). To confirm the potential for practical application, the anti-interference capabilities of the biosensor were tested. As shown in Fig. 5c, several biomolecules show no significant impact on the performance of the biosensor, validating its reliability for OP detection. Remarkably, its stability is confirmed with RGB values showing minimal decline after 15 days (Fig. 5d). Furthermore, the applicability of the biosensor for OP detection in real samples was evaluated. As shown in Table S4, the recovery rates of OPs range from 102.0% to 107.6%, demonstrating the high potential of this sensing platform for real-world OP detection.

Conclusions

In summary, this work achieves highly efficient glucose oxidation in acidic media by constructing a dual-site nanozyme composed of Fe single atom-bridged Au NPs, which serve as the binding sites for O_2 and glucose. The formation of metallic-bonded Fe–Au pairs enhances electron transfer and optimizes the electronic structure of active sites. Notably, *in situ* experiments and theoretical calculations reveal the presence of Au–Fe–OO intermediates during the reaction, which modifies the catalytic pathway, eliminates OH^- dependence, and enables efficient glucose activation under acid conditions. Benefiting from the aligned optimal conditions for both GOx- and POD-like activities at pH 4.0, an Au$_{NPs}$/FeNC-based glucose cascade system is successfully constructed. As a proof-of-concept, a portable biosensor kit based on this system is developed for real-time, ultrasensitive determination of OPs. This work advances the design of highly efficient nanozymes to meet the growing demands of practical applications.

Author contributions

Investigation, writing—original draft, X. L., and F. T.; providing help in measurements, Z. M., Y. Z. and Y. T.; investigation, C. W. and W. G.; funding acquisition, X. L., C. Z., and C. L.; supervision, writing—review & editing, J. L. and C. Z.

Conflicts of interest

There are no conflicts to declare.

Data availability

The data that support the findings of this study are available in the supplementary information (SI) of this article. Supplementary information: experimental details, additional characterizations, supplementary data, and supporting tables. See DOI: https://doi.org/10.1039/d5sc05430c.

Acknowledgements

The authors gratefully acknowledge the financial support of the National Natural Science Foundation of China (no. 22204045),

the Fundamental Research Funds for Hubei University of Technology (no. XBTK-2024007 and GCC2024013), the Fundamental Research Funds for the Central Universities (no. CCNU24JCPT032) and the Open Research Fund of the Key Laboratory of Ministry of Education, Hangzhou Normal University (KFJJ2023009).

Notes and references

1 W. Xu, L. Jiao, Y. Wu, L. Hu, W. Gu and C. Zhu, *Adv. Mater.*, 2021, **33**, 2005172.
2 X. Zhang, G. Li, G. Chen, D. Wu, Y. Wu and T. D. James, *Adv. Funct. Mater.*, 2021, **31**, 2106139.
3 D. M. Vriezema, P. M. L. Garcia, N. Sancho Oltra, N. S. Hatzakis, S. M. Kuiper, R. J. M. Nolte, A. E. Rowan and J. C. M. van Hest, *Angew. Chem., Int. Ed.*, 2007, **46**, 7378.
4 S. Liu and Y. Sun, *Angew. Chem., Int. Ed.*, 2023, **62**, e202308562.
5 Y. Li, R. Fu, Z. Duan, C. Zhu and D. Fan, *Small*, 2022, **18**, 2200165.
6 X. Jia, L. Jiao, R. Li, C. Chen, X. Li, L. Hu, Y. Zhai, C. Zhu and X. Lu, *Adv. Funct. Mater.*, 2024, **34**, 2406380.
7 L. Gao, H. Wei, S. Dong and X. Yan, *Adv. Mater.*, 2024, **36**, 2305249.
8 M. Zandieh and J. Liu, *Adv. Mater.*, 2024, **36**, 2211041.
9 S. He, L. Ma, Q. Zheng, Z. Wang, W. Chen, Z. Yu, X. Yan and K. Fan, *Bioact. Mater.*, 2024, **42**, 284.
10 Y. Zhou, W. Wei, F. Cui, Z. Yan, Y. Sun, J. Ren and X. Qu, *Chem. Sci.*, 2020, **11**, 11344.
11 R. Zhang, B. Jiang, K. Fan, L. Gao and X. Yan, *Nat. Rev. Bioeng.*, 2024, **2**, 849.
12 J. Chen, Q. Ma, M. Li, D. Chao, L. Huang, W. Wu, Y. Fang and S. Dong, *Nat. Commun.*, 2021, **12**, 3375.
13 W. Luo, C. Zhu, S. Su, D. Li, Y. He, Q. Huang and C. Fan, *ACS Nano*, 2010, **4**, 7451.
14 Z. Wang, R. Chen, W. Zhang, P. Sun, N. Zhang and Y. Zhao, *Adv. Funct. Mater.*, 2024, **35**, 2412767.
15 Y. Huang, M. Zhao, S. Han, Z. Lai, J. Yang, C. Tan, Q. Ma, Q. Lu, J. Chen, X. Zhang, Z. Zhang, B. Li, B. Chen, Y. Zong and H. Zhang, *Adv. Mater.*, 2017, **29**, 1700102.
16 Y. Wu, W. Xu, L. Jiao, W. Gu, D. Du, L. Hu, Y. Lin and C. Zhu, *Chem. Soc. Rev.*, 2022, **51**, 6948.
17 X. Cai, L. Jiao, H. Yan, Y. Wu, W. Gu, D. Du, Y. Lin and C. Zhu, *Mater. Today*, 2021, **44**, 211.
18 L.-H. Fu, C. Qi, J. Lin and P. Huang, *Chem. Soc. Rev.*, 2018, **47**, 6454.
19 Q. Wang, K. Chen, H. Jiang, C. Chen, C. Xiong, M. Chen, J. Xu, X. Gao, S. Xu, H. Zhou and Y. Wu, *Nat. Commun.*, 2023, **14**, 5338.
20 J. Chen, X. Liu, G. Zheng, W. Feng, P. Wang, J. Gao, J. Liu, M. Wang and Q. Wang, *Small*, 2023, **19**, e2205924.
21 Y. Wang, T. Chu, T. Jin, S. Xu, C. Zheng, J. Huang, S. Li, L. Wu, J. Shen, X. Cai and H. Deng, *Adv. Sci.*, 2024, **11**, 2308587.
22 B. Wu, H. Yang, L. Li, X. Tang, Y. Wu, B. Huang, D. Lutzenkirchen-Hecht, M. Qiu, K. Yuan and Y. Chen, *Adv. Mater.*, 2025, **37**, 2500096.
23 J. Zhang, Y. Yuan, L. Gao, G. Zeng, M. Li and H. Huang, *Adv. Mater.*, 2021, **33**, 2006494.
24 Y. Zhang, Q. Zhao, B. Danil, W. Xiao and X. Yang, *Adv. Mater.*, 2024, **36**, 2400198.
25 C. Wang, L. Wang, V. Nallathambi, Y. Liu, J. Kresse, R. Hübner, S. Reichenberger, B. Gault, J. Zhan, A. Eychmüller and B. Cai, *Adv. Mater.*, 2024, **36**, 2405200.
26 H. Shi, T. Wang, Z. Lin, S. Liu, X. Liu, R. Zhou, Z. Cai, Y. Huang and Q. Li, *Angew. Chem., Int. Ed.*, 2025, **64**, e202424476.
27 D. Jana, D. Wang, A. K. Bindra, Y. Guo, J. Liu and Y. Zhao, *ACS Nano*, 2021, **15**, 7774.
28 H. Wang, K. Wan and X. Shi, *Adv. Mater.*, 2019, **31**, 1805368.
29 H. Shen, S. Chen, S.-C. Mo, H. Huang, H. Liang, J. Zhang, Z.-L. Xu, W. Liu and Y. Liu, *Adv. Funct. Mater.*, 2024, **35**, 2418360.
30 X. Wang, Q.-Z. Li, J.-J. Zheng and X. Gao, *ACS Catal.*, 2024, **14**, 13040.
31 M. Comotti, C. Della Pina, E. Falletta and M. Rossi, *Adv. Synth. Catal.*, 2006, **348**, 313.
32 Y. Tang, X. Liu, P. Qi, W. Xu, Y. Wu, Y. Cai, W. Gu, H. Sun, C. Wang and C. Zhu, *Nano Lett.*, 2024, **24**, 9974.
33 X. Shen, W. Liu, X. Gao, Z. Lu, X. Wu and X. Gao, *J. Am. Chem. Soc.*, 2015, **137**, 15882.
34 K. Wang, Q. Hong, C. Zhu, Y. Xu, W. Li, Y. Wang, W. Chen, X. Gu, X. Chen, Y. Fang, Y. Shen, S. Liu and Y. Zhang, *Nat. Commun.*, 2024, **15**, 5705.
35 X. Luo, Z. Luo, S. Li, Q. Fang, W. Xu, H. Wang, Y. Wang, G. M. Bao, W. Gu and C. Zhu, *Anal. Chem.*, 2023, **95**, 12306.
36 Y. Yang, Y. Xiao, L. Jiang, J. Li, J. Li, J. Jia, C. T. Yavuz, F. Cui, X. Jing and G. Zhu, *Adv. Mater.*, 2024, **36**, 2404791.
37 X. Wei, S. Song, W. Cai, X. Luo, L. Jiao, Q. Fang, X. Wang, N. Wu, Z. Luo, H. Wang, Z. Zhu, J. Li, L. Zheng, W. Gu, W. Song, S. Guo and C. Zhu, *Chem*, 2023, **9**, 181.
38 Q. Li, S. Wu, B. Li, P. Zhou, H. Wang, X. Zhang, Q. Meng, X. Li, H. Chen, Y. Pang and R. Chen, *Small*, 2024, **20**, 2405321.
39 J. Yu, T. Chen, X. Wen, H. Shi, L. Wang and Y. Xu, *Biosens. Bioelectron.*, 2024, **253**, 116169.
40 Y. Tang, Y. Chen, Y. Wu, W. Xu, Z. Luo, H.-R. Ye, W. Gu, W. Song, S. Guo and C. Zhu, *Nano Lett.*, 2023, **23**, 267.
41 E. G. Mahoney, W. Sheng, M. Cheng, K. X. Lee, Y. Yan and J. G. Chen, *J. Power Sources*, 2016, **305**, 89.
42 C. Feng, Z. Zhang, D. Wang, Y. Kong, J. Wei, R. Wang, P. Ma, H. Li, Z. Geng, M. Zuo, J. Bao, S. Zhou and J. Zeng, *J. Am. Chem. Soc.*, 2022, **144**, 9271.
43 K. Kunimatsu, T. Yoda, D. A. Tryk, H. Uchida and M. Watanabe, *Phys. Chem. Chem. Phys.*, 2010, **12**, 621.
44 Y. Zhou, Y. Wu, Z. Luo, L. Ling, M. Xi, J. Li, L. Hu, C. Wang, W. Gu and C. Zhu, *J. Am. Chem. Soc.*, 2024, **146**, 12197.
45 W. Xu, Y. Wu, X. Wang, Y. Qin, H. Wang, Z. Luo, J. Wen, L. Hu, W. Gu and C. Zhu, *Angew. Chem., Int. Ed.*, 2023, **62**, e202304625.
46 X. Li, W. Tan, J. Fan and K. Li, *ACS Nano*, 2024, **18**, 24162.
47 M. Lei, X. Ding, J. Liu, Y. Tang, H. Chen, Y. Zhou, C. Zhu and H. Yan, *Anal. Chem.*, 2024, **96**, 6072.
48 Y. Wu, L. Jiao, X. Luo, W. Xu, X. Wei, H. Wang, H. Yan, W. Gu, B. Z. Xu, D. Du, Y. Lin and C. Zhu, *Small*, 2019, **15**, e1903108.